EVALUATION OF AN EXPERIMENTAL DATA SET TO BE VALIDATION DATA FOR CFD FOR A VHTR

Richard W. Johnson

Idaho National Laboratory, Idaho Falls, Idaho, USA

Abstract

The very high temperature reactor (VHTR) has been chosen as the concept for the next generation nuclear plant (NGNP), supported by the U. S. Department of Energy. There are two basic designs for the VHTR: a prismatic design and a pebble-bed design. In the prismatic design, the coolant (helium) exits the core into a lower plenum as jets. The helium then turns 90° and flows toward the exit duct around cylindrical support posts. Safety analysis by computational fluid dynamics (CFD) is desired to determine the level of mixing of the jets and check for hot spots. Experimental data were taken in a scaled model of a slice of the lower plenum of a prismatic VHTR. Numerical investigations have been made using CFD to determine if the data are suitable for validation. This paper provides the findings of the investigations including results for a modified version of the flow field. The investigations include a determination of the extent of the computational domain needed, the best outlet boundary condition to use, the accuracy of the inlet data, application of several turbulence models and the search for the cause of an instability that causes large random excursions of flow variables. It is found that the inlet data measured by PIV are not sufficiently accurate and that the instability is apparently caused by the presence of the first inlet jet which impinges on a recirculation zone.

1. INTRODUCTION

After traversing the VHTR core, the heated gas enters the lower plenum as jets where it mixes and exits the reactor vessel. The heat generation in the core is not uniform, leading to coolant jets of varying temperatures. Figure 1 gives a plan view of ½ of the prismatic VHTR lower plenum showing numerous cylindrical support pillars, locations of jet inlets (smaller circles amongst the pillars) and the exit duct. There are concerns that the heated helium may create hot spots in the lower plenum of the reactor vessel. There is also concern that the helium will not be sufficiently mixed to attain a uniform temperature as it exits the reactor vessel. The application of a CFD code to characterize the helium flow in the lower plenum requires that the calculations be validated against experimental data.

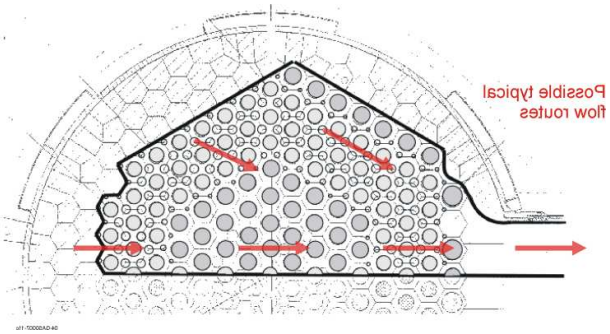

Figure 1. Plan view of the VHTR lower plenum.

Isothermal experimental data have been taken using stereo particle image velocimetry (PIV) in the Idaho National Laboratory's matched index of refraction (MIR) facility for a 1:6.55 scaled model of a narrow section of the lower plenum (MacIlroy et al., 2008). Figure 2 provides isometric and plan views of the scaled model, showing inlet ports, half and full cylindrical posts, the exit plane and the origin and coordinate axes used for the CFD model. The half cylinders are included in the scaled model because the model was designed as an exact scaled replica. The inner model geometry is 53.98

mm wide, 558.8 mm long with the first jet located at 88.93 mm from the origin, and 217.5 mm high. Diameters for the inlet jets and posts are 0.0221 mm and 0.03175 mm, respectively.

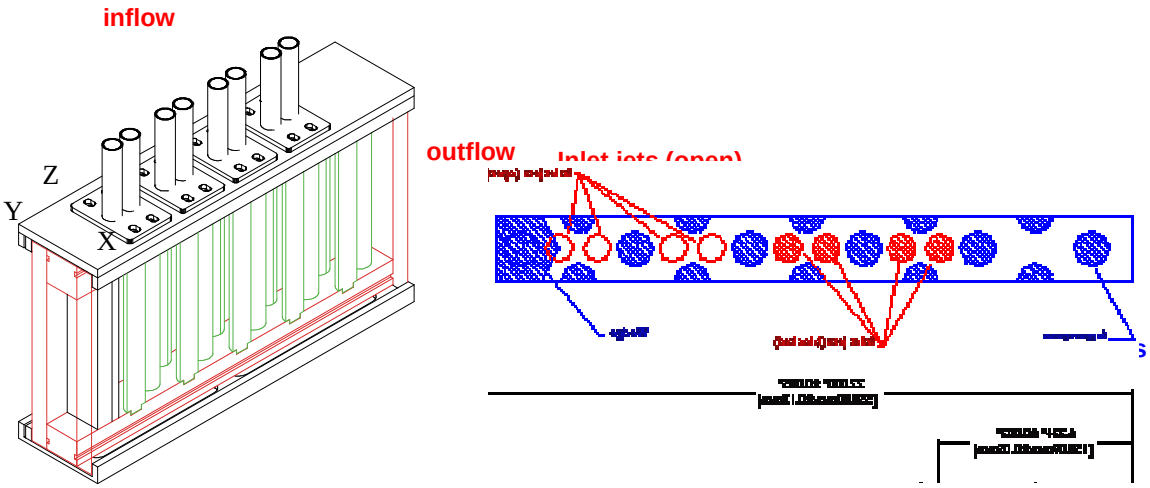

Figure 2. Isometric and plan views of the scaled model and coordinate axes for the CFD model.

The overall objective of the CFD study of the scaled model is to investigate issues related to the suitability of the experimental data for use as a validation data set. These issues include the suitability of the model geometry, how many inlet jets should be employed, how sensitive the internal flow is to the symmetry/asymmetry of the inlet jets and how complex the flow actually is. Other issues include the completeness and accuracy of the inlet conditions and whether the flow involves vortex-shedding. Three dimensional CFD calculations have been made to investigate these issues for a jet inlet Reynolds number = $\overline{u}\, d_{jet}/\nu$ = 12,400, where $\overline{u}$ is the bulk velocity of the jet. The study employs the Reynolds-averaged Navier-Stokes (RANS) turbulence models for the investigation of the MIR data.

2. NONSTATIONARY TURBULENT FLUID DYNAMICS

Turbulent flow is characterized by random fluctuations in all three spatial directions. In addition to these motions, there may be additional unsteady motions that are not from turbulence. Such flows are termed nonstationary. Examples of these include turbulent flow in turbomachinery where there is unsteadiness from rotating blades, turbulent flow around bluff bodies that causes vortex-shedding and turbulent flow that is being pumped by a pulsating pump. In the present case, it is assumed that the flow around the cylindrical posts generates vortices. For nonstationary turbulent flow, two averaging operations can be applied to the instantaneous flow quantities (Johnson, 2008a). First, the random turbulence is averaged out of the Navier Stokes equations by performing an ensemble average. The procedure is called Reynolds averaging and the resulting equations are called the Reynolds-averaged Navier Stokes (RANS) equations. An approach that employs the unsteady RANS equations is called a URANS approach. Mathematically, for nonstationary flow the instantaneous quantities are decomposed into an ensemble average and a random fluctuating component. For example, for the X-component of velocity:

$$u = \langle u \rangle + u' \tag{1}$$

where $\langle u \rangle$ is the ensemble average and u' is the turbulent fluctuation. The ensemble average can vary in time because of non-turbulent unsteadiness. The ensemble-averaged quantity can be decomposed further into a time-averaged component and a coherent fluctuation. The coherent fluctuation is related to non-turbulent unsteadiness such as vortex-shedding. For example

$$\langle u \rangle = U + \tilde{u} \tag{2}$$

where U is the time average of the ensemble average (or long-time average or just time mean) and $\tilde{u}$ is the coherent fluctuation. These averaging processes are applied to the velocity components and

pressure. The velocity components are given as *u, v* and *w* in the X, Y and Z directions, respectively. The present CFD simulations compute the ensemble averages. These are concurrently time-averaged (by a running time-averaging calculation) because the experimental data of McIlroy et al. (2008) are long-time averaged. Furthermore, the data were taken at a rate of 2 - 3 data planes per second, which is insufficiently rapid to capture the vortex shedding. However, the data were taken for time intervals of about 375 seconds such that a fairly representative long-time average should have been obtained.

3. CFD MODELS

3.1 Flow Domain and Outlet Boundary Condition

The 104.8 mm wide scaled model was positioned inside the test section of the INL's MIR facility, which has a cross section of 609.6 mm square. The mineral oil working fluid not only flows into the scaled model, but also around the outside of the model. A concern was that the outer flow would alter the flow at the exit of the scaled model, possibly affecting the flow inside the model. A two-dimensional study, using a URANS approach, was performed to assess the effects of the outer flow on the inner flow and determine if the outer flow should be included in the CFD model (Johnson, 2008b). The commercial CFD code FLUENT (2008) was used in the 2-D study. The Reynolds stress transport turbulence model (RSM) was employed. Mesh and iterative convergence were achieved.

Figure 3 illustrates the geometry and streamlines for the 2-D case where both inside and outside flows are included. As can be seen, the flow develops shedding vortices around the full and half cylinders inside the model; it can also be seen that there are vortices forming beyond the 25.4 mm thick walls of the scaled model. It was found that because of the vortex shedding from the last cylinder there is inflow at the exit plane of the scaled model.

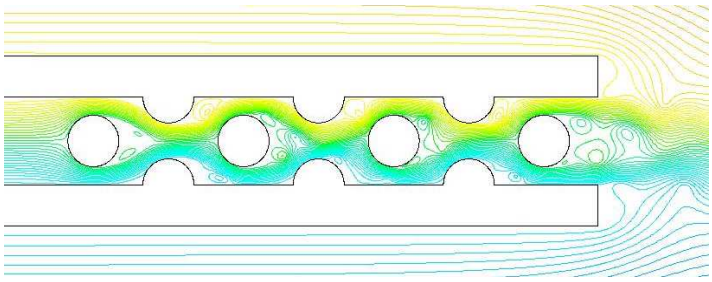

Figure 3. Stream function contours of the flow in the 2-D CFD model that includes the outer flow.

Additional 2-D cases were computed where only the inner flow was included and where two different boundary conditions were employed at the outlet plane. The two boundary conditions used were the 'outflow' and 'pressure-outlet' conditions. These two boundary conditions are available in both commercial CFD codes FLUENT (2008) and STARCCM+ (2008). The 'outflow' boundary condition enforces a constant gradient condition for the velocity components while the 'pressure-outlet' condition sets a constant static pressure just downstream of the outlet plane. Actually, neither of these conditions is exactly correct because of the vortex shedding behind the last post.

Figure 4 illustrates the time mean streamwise velocity *U* at the outlet plane and at profile location '3f,' (see Fig. 3), for cases employing the 'outflow' and the 'pressure-outlet' conditions compared to the reference case, which includes the outer flow (inner-outer). As can be seen, the three cases are distinctly different at the outlet plane. However, at location 3f, results for the 'pressure-outlet' case compare very closely with the reference case. Figure 5 compares the three cases for time mean transverse velocity *V* and the kinematic Reynolds stress $\overline{uv}$ at 3f. As shown, the 'pressure-outlet' results closely match those for the reference case. These results provide confidence that including only the flow domain inside the scaled model along with using the 'pressure-outlet' boundary condition will not cause inaccuracy in the results except in the region very close to the outlet plane.

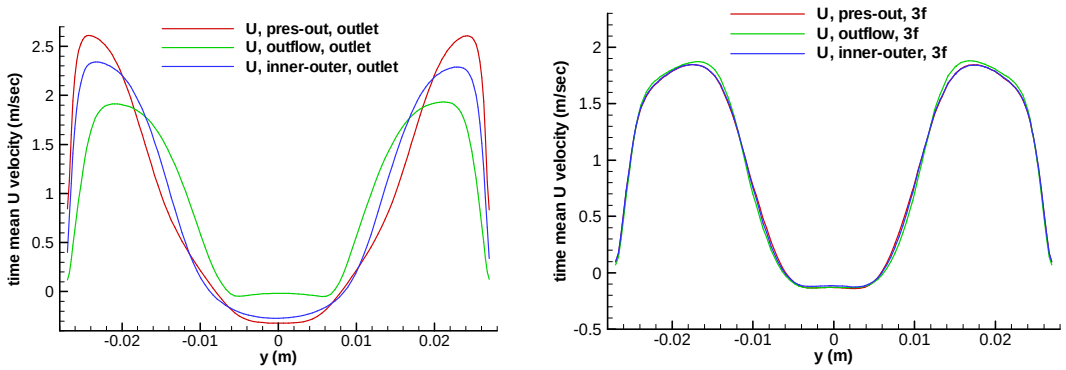

(a) (b)

Figure 4. Profiles of the time mean velocity *U* at (a) the outlet plane and at (b) location 3f (Fig. 3).

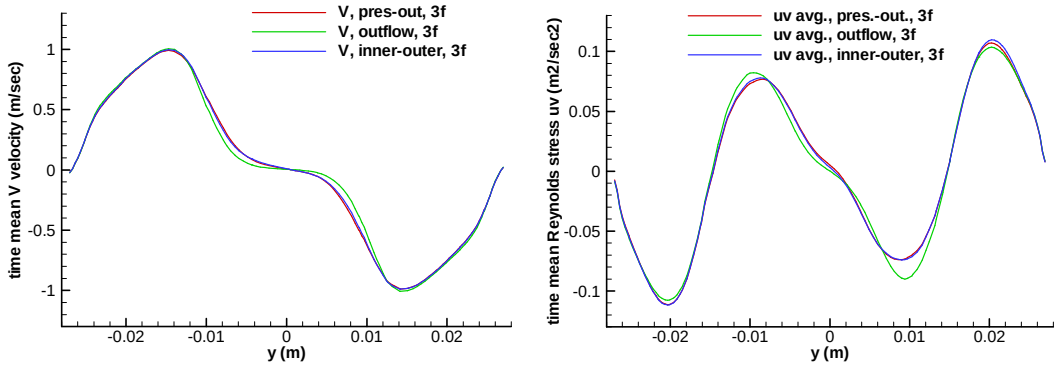

(a) (b)

Figure 5. Profiles of (a) the time mean velocity *V* and (b) the Reynolds stress $\overline{u}\overline{v}$ at 3f (Fig. 3).

3.2 Inlet Conditions

Accurate and complete inlet boundary conditions are critical to the usefulness of any CFD validation data set. These include the velocity components and turbulence parameters, usually the turbulent kinetic energy (TKE). The inlet mass flows for the experiment were adjusted and measured by calibrated mass flow rotameters, one for each inlet duct. The mass flow to the first jet was set to be two-thirds that of the others because of the smaller flow area (see Fig. 2). The rotameters provided accurate mass flow rates. Additionally, PIV data were taken for a vertical stretch of the inlet ducts of the scaled model. Three-dimensional velocity data were taken in eleven 2 mm thick X-Z planes illuminated by laser sheets. Data at Z = 9.7 and 11 mm were extracted for use as inlet conditions.

The inlet data were read as tables into STARCCM+. Values were interpolated onto the grid and then integrated to obtain the mass flow rates. Unfortunately, the reduced PIV data do not generally compare well with the mass flow rotameter data, Johnson (2009). Table 1 provides information on the percent difference the mass flows based on the PIV data are from the rotameter data.

Table 1. Percent difference of mass flows from measured rotameter values for the PIV-based flows.

	jet 1	**jet 2**	**jet 3**	**jet 4**	**total**
PIV @ 9.7 mm	25.1% low	7.98% low	4.46% low	8.99% low	10.4% low
PIV @ 11 mm	18.1% low	0.78% low	2.99% low	8.80% low	6.70% low

Clearly, there are some significant differences between the rotameter data and the mass flows, in particular for Jet 1. Greater confidence in the PIV-measured inlet data would be obtained if the differences from the rotameter data were less than 5%. This is actually true for jet 3 at 9.7 and 11 mm and Jet 2 at 11 mm. However, there are also significant differences between the PIV inlet data from

9.7 to 11 mm for Jets 1 and 2, which casts further doubt on the accuracy of the PIV-based inlet data. It was decided that the best approach for the inlet conditions is to use the rotameter data to compute bulk velocity in the Z-direction, set the other two velocities to zero and match the TKE in the core of the inlet ducts to the MIR data. The inlet data are applied at Z = 88.5 mm, which is the height of the inlet ducts. Just above this level are turbulence generating screens preceded by flow straighteners.

3.3 Meshing

In the aforementioned 2-D study (Johnson, 2008b), three different grids of increasing fineness were employed. It was found that the intermediate and finest grid yielded very similar results. For the 3-D meshes, two 2-D grids were constructed based on the coarsest and intermediate 2-D grids above, then extruded vertically. Inlet ducts of 88.5 mm were added to the coarser grid, denoted a4. The number of cells in the Z-direction is 100 in the inlet ducts and 110 cells in the main body for a total of 5.8 million cells. Though it was intended to use the finer grid for final data comparison, it was decided to use the coarser grid for initial investigations of the MIR data. GAMBIT 2.4.6, which comes with FLUENT, was used to create the meshes. Figure 6 shows a detail of grid a4 plus an isometric view. The inlet jet ports are green, the outlet plane is red and the walls are gray.

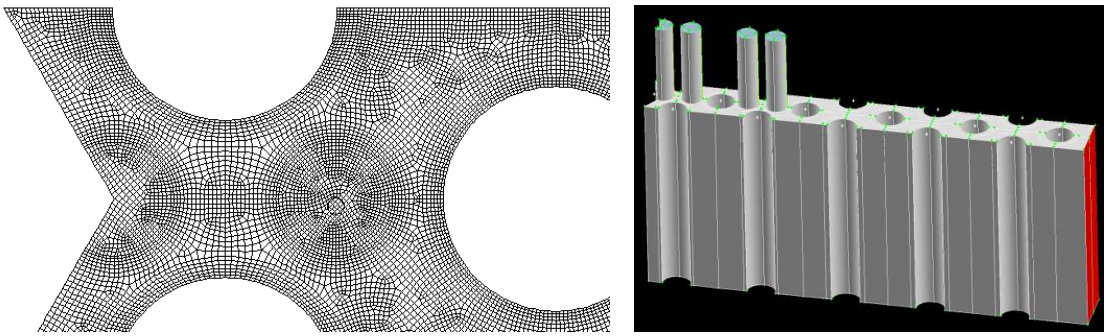

Figure 6. A detail of the cross-section and an isometric view of grid a4.

3.4 Computational Details

The commercial CFD code STAR-CCM+ was used for the 3-D computations. The best practice guidelines used in the present study consist of those specified for the ASME Journal of Fluids Engineering. The flow problem is set up using a URANS approach, because of the expectation of vortex shedding. Second-order differencing is used for both spatial and the implicit temporal discretization; the segregated solver is used. Walls are considered smooth and are assigned the no-slip condition. Simulations using grid a4 employ a time step of 2.0×10^{-4} second. The 'pressure-outlet' boundary condition is used at the outlet as discussed above. The iterative convergence for each time step was set based on the calculation of a Poiseuille flow, which has an analytical solution. It was found from the Poiseuille flow calculation that a residual computed in STARCCM+ in the default mode is converged at a value of about 2×10^{-4}.

Figure 7 illustrates profile locations in the scaled model that will be referred to for data comparisons. The profiles shown in the plan view each represent two profiles: one at Z = -0.07 m (given suffix 'u') and one at Z = -0.15 m (suffix 'd'). So for example, profile 'x1d' is at location 'x1' at Z = -0.15 m, while 'p2u' is at point p2 at Z = -0.07 m.

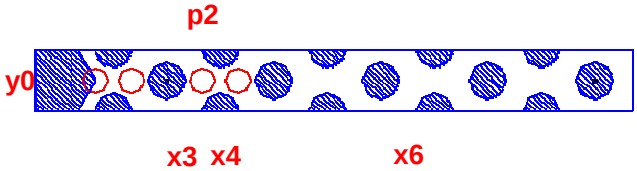

Figure 7. Locations of profiles and points for data comparison.

The CFD calculations must be long-time averaged to compare with the MIR data, which are averaged over 375 seconds. The long-time averaging is computed concurrently with the unsteady calculations. The question arises as to how long the simulation must be carried out to provide an unchanging long-time average. Figure 8 plots the time mean velocity *W* along profile 'y0u,' for five points in time. Grid a4 and the SST $k\sim\omega$ turbulence model and uniform inlet profiles are used. This profile captures the four jet inlets along the centerline. Computations for 2.4 seconds or less are significantly different from longer time averages in the region of the first jet. These results actually are an indication that there is some kind of instability in the vicinity of Jet 1. This instability is investigated further below. It is concluded that calculations need to run for at least 3 seconds.

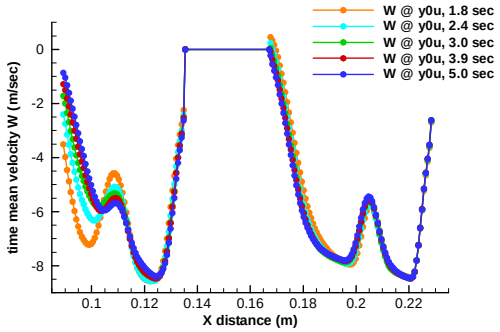

Figure 8. Time mean velocity *W* along data profile 'y0u' at five different times.

3.5 Initial Conditions

Two methods for beginning the unsteady calculations were investigated. The first method is to begin a steady calculation until the residuals stop decreasing, then initiate unsteady calculations. The second is to start from a stagnant condition. Computations were made using the AKN $k\sim\varepsilon$ turbulence model starting from these two initial conditions. Differences in results were not significant compared to differences using different turbulence models, Johnson and Schultz (2009).

3.6 Turbulence Models

RANS turbulent models are employed to represent the turbulence in the flow. Any turbulence model that is to be used for reactor safety analysis must be validated for the range of phenomena to which it is to be applied. The behavior of the turbulence model in the near-wall region is important because its large effects on wall friction and heat transfer. A nonturbulent region exists adjacent to the wall and has been found experimentally to be where the dimensionless wall distance $y^+ = yu_\tau/\rho < 11$. Here y is the dimensional distance, u_τ is the friction velocity defined as the square root of the wall shear stress divided by the density ρ, and μ is the dynamic viscosity. Some turbulence models require the additional specification of a wall treatment while others are designed to intrinsically apply all the way to the wall. The near-wall y^+ values for grid a4 are mostly between 1 and 12 and therefore in the viscous region or sublayer. This is appropriate for turbulence models that are designed to handle the viscous sublayer. However, standard wall functions are also designed to work within the viscous sublayer. Four turbulence models are employed within STARCCM+ in the present study. These are the Reynolds stress transport turbulence model (RSM) with the two layer all $y+$ wall treatment, the standard $k\sim\varepsilon$ (SKE) two layer model with the all y^+ wall model, the Abe-Kondoh-Nagano (AKN) $k\sim\varepsilon$ low Re model with the all y^+ wall model and the Menter shear-stress transport $k\sim\omega$ model (SKW) with the all y^+ wall model. The latter two models are specifically designed to apply up to the wall.

4. RESULTS AND DISCUSSION

4.1 Detailed Results for Four Jets

Results are obtained for the four turbulence models described above. The inlet conditions are based on the rotameter data as mentioned. The turbulent kinetic energy and turbulent dissipation rates are set to 0.1 J/kg and 1.0 J/kg-sec for all jets for the RSM, SKE and AKN models. For the SKW, the inlet turbulent kinetic energy is the same while the specific dissipation rate is set to 1.0 sec^{-1}. All cases

use grid a4 and are computed to 5 seconds, except for the SKE case, which becomes periodic and is cut off at 3.7 seconds. The long-time averages are performed over the five seconds, except for SKE, where it is performed over four periodic cycles.

Figure 9 plots time mean results for vertical velocity *W* for the four turbulence models for profiles y0u and y0d. The four jet signatures are clearly visible in the data at y0u. The calculations are poorest near Jet 1, but improve until they match the signature for Jet 4 for all four turbulence models. Calculations for profile y0d are quite similar for all cases, though the signature for Jet 1 is missing.

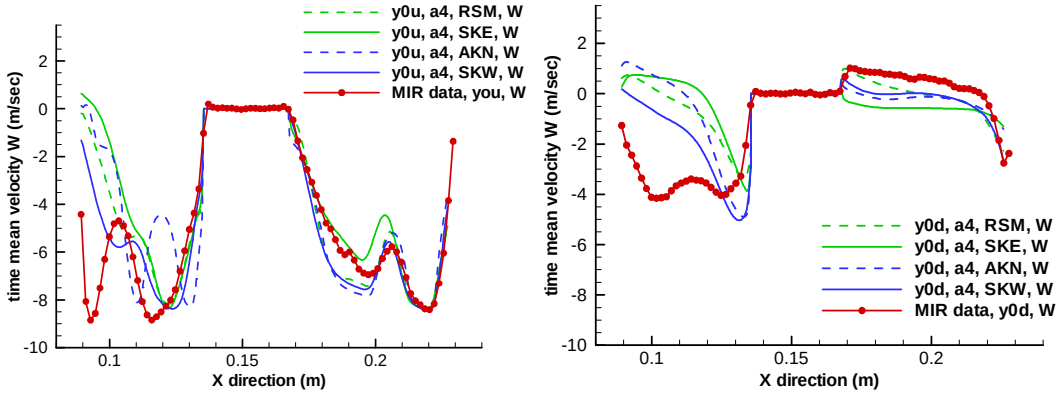

Figure 9. Time mean velocity *W* at y0u and y0d.

Figure 10 compares results for the four turbulence models with the MIR data at profiles x3u, x3d, x4u, x4d, x6u and x6d. At x3u, just upstream of Jet 3, the flow is mostly vertical and the results differ significantly. At x3d, the flow has turned and become mostly horizontal. The spikes seen at x3 in the MIR data are not present in the calculations. The flow accelerates at x4 because of the presence of the two half posts. Again, the computed results vary widely, though the SKW results look best overall. By profile x6, the effects of the jet inflow have reduced considerably and all of the results are showing correct trends. Overall, the calculations in the vicinity of the inlet jets show the poorest agreement.

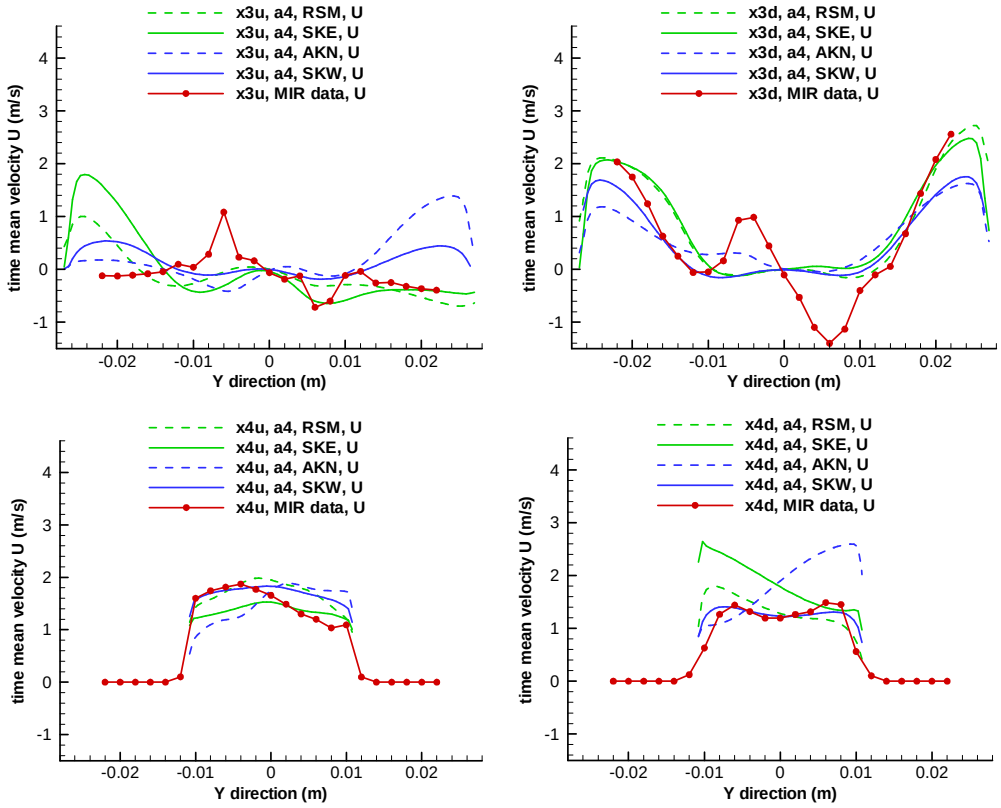

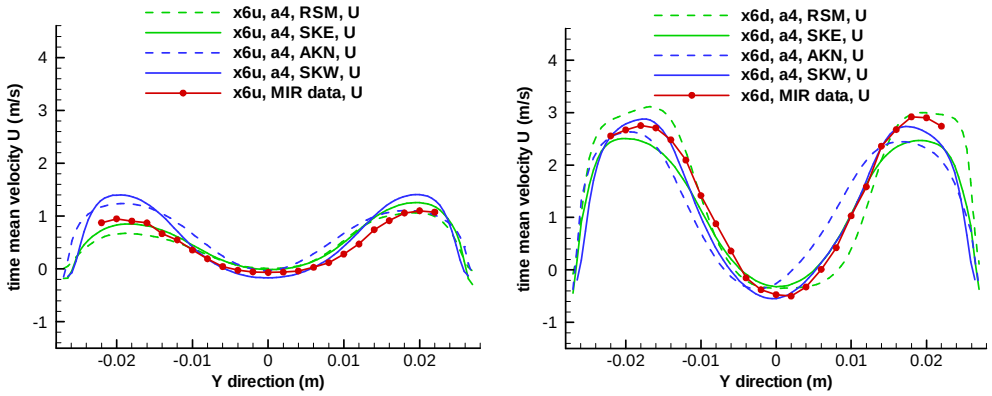

Figure 10. Comparison of time mean velocity *U* results for the four cases with the MIR data.

Figure 11 plots time evolution curves for the computed ensemble mean velocity <*w*> at point p2u for the four turbulence models. This point is located in the center of Jet 3 at Z = -0.07 m. All of the results do show periodic behavior. However, only the SKE and the RSM show well-behaved periodic behavior. The traces for AKN and SKW exhibit dramatic variations that appear to be random in time.

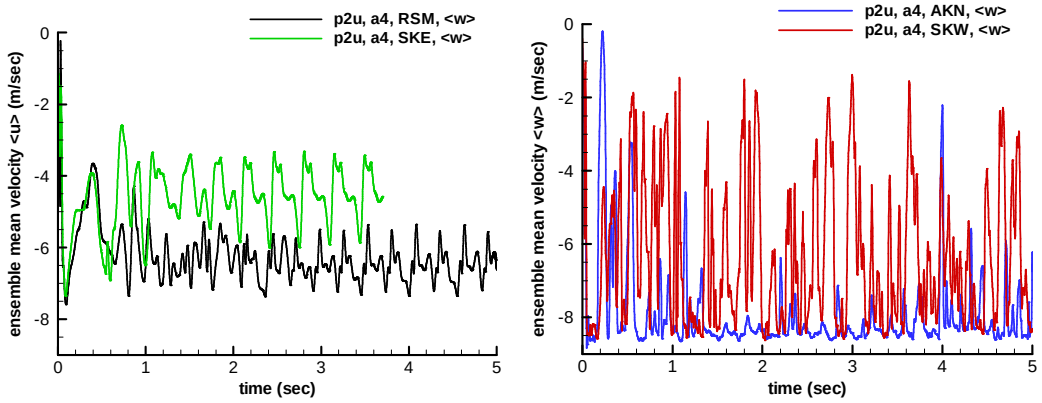

Figure 11. Time traces at point p2u for the four turbulence models.

Figure 11 suggests that the four turbulence models produce different levels of turbulent viscosity because of the varying levels of damping of the time traces. In fact, when contour levels of the ratio of turbulent to molecular viscosity are plotted for the end times of the computations at Z = -.07 m, Fig. 12, it is seen that the RSM and SKE, which both show well-behaved periodicity in Fig. 11 have similar relatively high levels, while the AKN has lower levels and the SKW has the lowest levels.

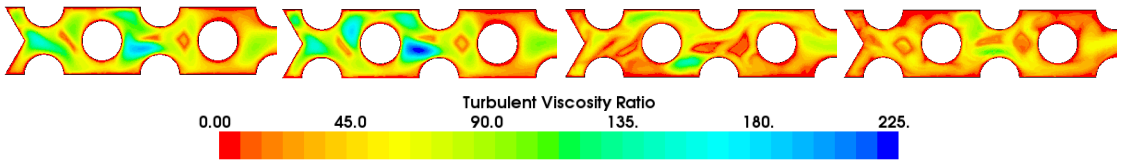

(a) (b) (c) (d)

Figure 12. Turbulent to molecular viscosity ratio for the (a) RSM, (b) SKE, (c) AKN and (d) SKW.

It is also interesting to compare contours of time mean vertical velocity *W* for the four cases to obtain an overall picture of how well the flow is predicted. Figure 13 illustrates contours for *W* at Z = -0.07 m. Signatures of the four jets are visible in the plots. As can be seen, the RSM and SKE cases show similar asymmetric contours with Jet 1 skewed to one side; the AKN shows a skewing in the opposite sense, while the SKW shows a very symmetric solution. Apparently, the four turbulence models have "found" differing solutions. This may be because the flow is so unstable that there is no actual periodically stable solution. Also, the skewed results for Jet 1 explain the absence of a signature for Jet 1 in Fig. 9 for the RSM, SKE and AKN models. For SKW, the Jet 1 signature is quite small.

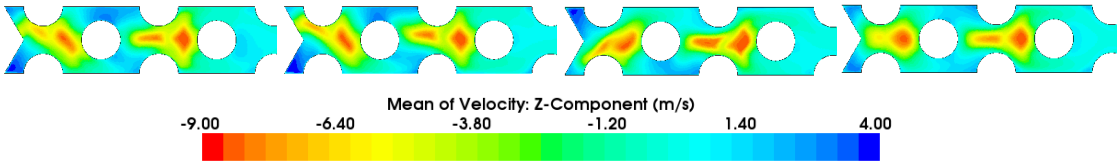

(a) (b) (c) (d)

Figure 13. Contours of mean velocity *W* at Z = -0.07 m for (a) RSM, (b) SKE, (c) AKN and (d) SKW.

The MIR data show symmetry in the contours of *W* at Z = - 0.07 m, Fig. 14, indicating that the SKW model gets the more correct solution. Note that the range of contour levels is the same for all graphics.

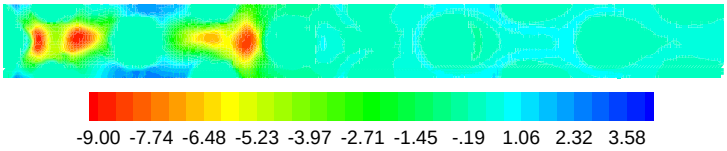

Figure 14. Contours of time mean velocity *W* at Z = - 0.07 m from the MIR data.

Additional investigations have shown that an unstable recirculation zone is present below Jets 1 and 2, Johnson et al. (2010). Figure 15 illustrates streamlines calculated at specific points in time for the SKW model. As can be seen, the recirculation zone below the first two jets changes dramatically in time. The flow from the two jets is seen to detach from the left wall flowing outwards and then back around in a recirculation flow which then impinges upwards on the jets flowing downwards. This mutual impingement is apparently what causes the recirculation zone to change in time because of its instability. Also, the instability is predicted to be random in time as can be seen in Fig. 11.

In comparing the results for the four turbulence models, it is interesting to observe that the three with the highest turbulent viscosity levels have found inappropriate solutions for the first two jets. It may well be the case that the turbulence level in the scaled model is not very high, even though the inlet jets have a Reynolds number of 12,400, well in the turbulent range. It is the low viscosity SKW model that shows the most appropriate behavior.

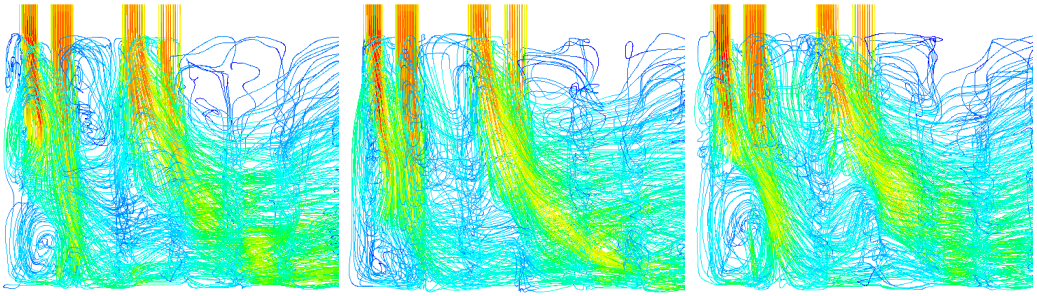

Figure 15. Streamline plots for the SKW case at 3.6, 3.9 and 4.2 seconds, respectively.

4.1 Detailed Results for Three Jets

Figure 16a illustrates time traces from the MIR data at point p2u. The range of variation of the amplitude for *w* is even greater than for the SKW calculations, Fig. 11. These high amplitude oscillations are apparently a result of the unstable recirculation zone. It was decided to investigate the flow field for the case of shutting off Jet 1, inasmuch as it impinges on the recirculation zone and may be the cause of its random instability. Figure 16b provides time traces for calculations for the same four turbulence models for point p2u with Jet 1 shut off; compare to Fig. 11. Calculations of the time traces for all four models now show very low or no oscillations, indicating that the instability has disappeared. Streamline plots of the flow using the SKW model show a large recirculation zone that appears to be stable at three different calculation times, see Johnson et al. (2010). Figure 17 provides predictions for the *three-jet* cases for *W* at y0u and y0d and *U* at x3u, x3d, x4u, x4d, x6u and x6d compared to the *four-jet* MIR data. The long-time averages do not include the initial transients.

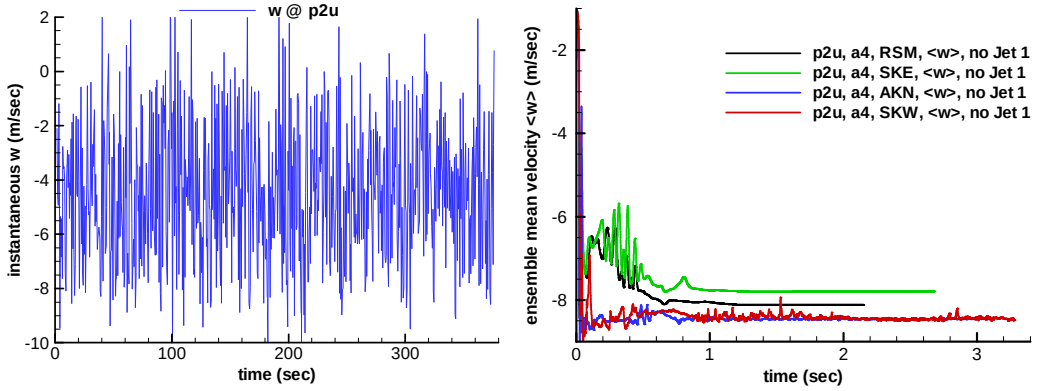

(a) (b)

Figure 16. Time traces for point p2u for (a) the MIR *data* with four jets active and (b) *calculations* for four turbulence models for Jet 1 turned off.

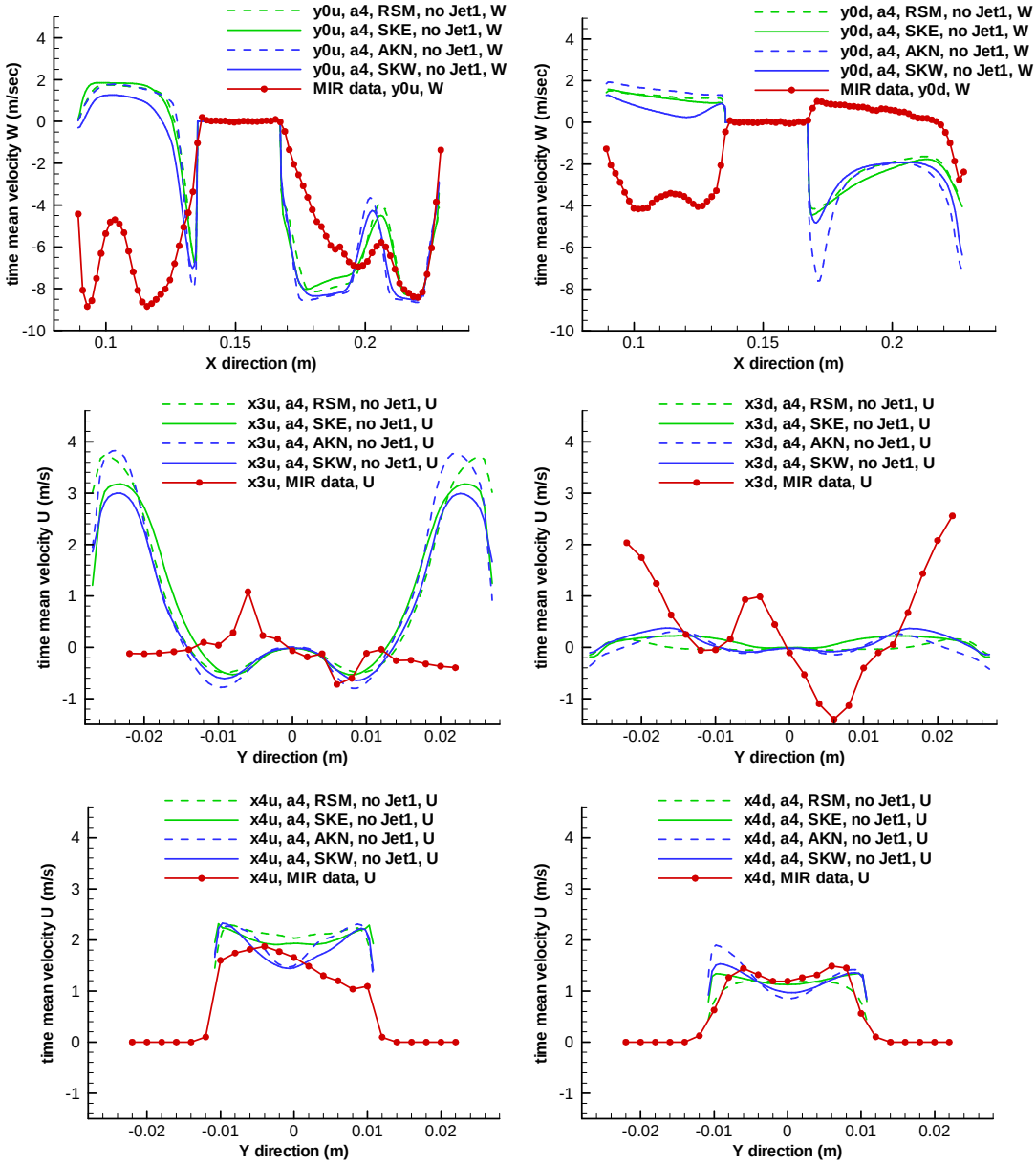

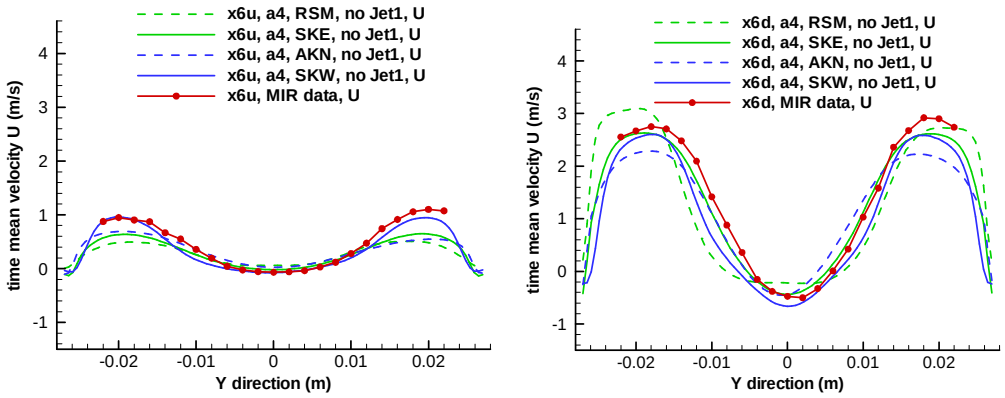

Figure 17. Blind predictions for time mean profiles for Jet 1 turned off (MIR data for Jet 1 active).

Clearly, the calculations for the four turbulence models for the three-jet case are much closer to each other than for the four-jet case. The signatures of the three remaining jets at y0 have changed significantly. At x3u and x3d, predictions are now the reverse of what the four-jet data show. Calculations at x4u are all symmetric in contrast to the four-jet data. The predictions for x4d, x6u and x6d are fairly close to the four-jet data, especially for the latter two, as the influence of the jets has diminished significantly. Figure 18 illustrates contours of *W* in the vicinity of the inlet jets at Z = -.07 m. The jet signatures are clearly visible and are all quite symmetric and quite similar.

It has been seen that two significant objections have been identified and discussed for the existing MIR data to be used for validation data. These are the discrepancy between the measurements of inlet mass flow between the calibrated rotameters and the detailed PIV data and the presence of an unstable and randomly varying recirculation zone in the bottom corner of the model below the first two jets. The reasons that the presence of the unstable zone makes the data unsuitable are first that the instability appears to be random in time such that there may not be a periodically stable solution and second that the time scale of the change of the zone is about an order of magnitude longer than the time scale of shedding vortices, Johnson (2010), making it very impractical to compute because of the long simulation time that would be needed. It seems far more appropriate to validate a CFD model for the case of no Jet 1 and then apply it to the problem of the four-jet data to see if it can be calculated. It is recommended that the MIR data be retaken with improved accuracy for the inlet conditions and with Jet 1 turned off.

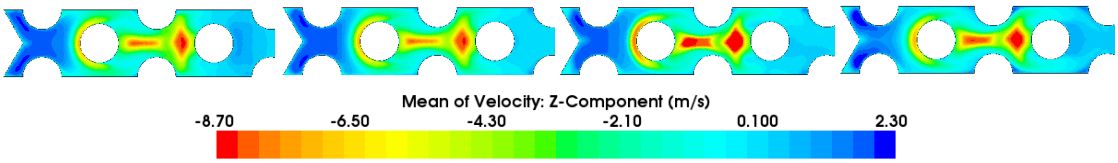

Figure 18. Contour plots of *W* at Z = -0.07 m for the RSM, SKE, AKN and SKW for no Jet 1.

5. SUMMARY AND RECOMMENDATIONS

Experimental data were earlier taken in the INL's MIR test facility for a scaled section of the lower plenum of a prismatic VHTR with the objective of providing a CFD validation data set. The present report provides a summary of CFD simulations performed to investigate the suitability of the data for validation purposes. Important findings include the observation that inlet data taken using PIV do not match the flow rates measured by calibrated rotameters. This discrepancy is a serious shortcoming of the MIR data and should be remedied. Present calculations were made using the rotameter data for inlet conditions. Four turbulence models were used to simulate the MIR data: the standard $k\sim\varepsilon$ two-layer model, the AKN low Re $k\sim\varepsilon$ model, the Menter SST $k\sim\omega$ model all with all y^+ wall treatments and the Reynolds stress transport model (RSM) with the two layer all $y+$ wall treatment. Time trace results from the $k\sim\omega$ model indicate that an unstable recirculation zone present below Jets 1 and 2 causes significant perturbation to the flow field with an apparently random time

scale. CFD calculations show large differences amongst the four models and the data. Calculations made with Jet 1 turned off indicate that the unstable zone has been stabilized and that CFD results for the four models are more closely matched. The calculations represent blind predictions for flow in the scaled model. It is recommended that the MIR data be retaken with improved accuracy for the inlet conditions and with Jet 1 turned off. Finally, it is clear from the above CFD investigation that CFD should be used in the design of new validation data sets.

6. ACKNOWLEDGEMENTS

Work supported by the U.S. Department of Energy, Office of Nuclear Energy, under DOE Idaho Operations Office Contract DE-AC07-05ID14517.

7. REFERENCES

ASME Journal of Fluids Engineering: http://journaltool.asme.org/Templates/JFENumAccuracy.pdf

FLUENT, version 6.3.26, FLUENT Inc., 10 Cavendish Court, Centerra Resource Park, Lebanon, NH, 03766 (2008).

H. M. McIlroy, D. M. McEligot and R. J. Pink, Measurement of Flow Phenomena in a Lower Plenum Model of a Prismatic Gas-Cooled Reactor, *Proceedings of the 16th International Conference on Nuclear Engineering (ICONE-16)*, Orlando, May 11-15 (2008).

R. W. Johnson, "Modeling Strategies for Unsteady Turbulent Flows in the Lower Plenum of the VHTR," *Nuclear Engineering & Design*, **238**, 482-491 (2008).

R. W. Johnson, Development of a CFD Analysis Plan for the First VHTR Standard Problem, *Proceedings of the 4th International Topical Meeting on High Temperature Reactor Technology (HTR2008)*, paper HTR2008-5828, Washington, D. C., Sept. 28 – Oct. 1 (2008).

R. W. Johnson and R. R. Schultz, Computational Fluid Dynamic Analysis of the VHTR Lower Plenum Standard Problem, Idaho National Laboratory report INL/EXT-09-16325 July (2009).

R. W. Johnson, Examination of a Proposed Data Set Using CFD Calculations, *Proceedings of the ASME 2009 Fluids Engineering Summer Meeting (FEDSM2009)*, paper FEDSM2009-78317, Vail, Colorado, August 2 – 5 (2009).

R. W. Johnson, H. M. McIlroy, R. C. Johnson and D. P. Christensen, Undesirable Flow Behavior in a Proposed Validation Data Set, Paper ICONE18-29474, *Proceedings of the 18th International Conference on Nuclear Engineering (ICONE18)*, Xi'an, China, May 17-21 (2010).

STAR-CCM+, version 3.04, 20, CD-adapco, 60 Broadhollow Road, Melville, NY 11747 (2008).